

Investigation of the annealing temperature dependence of the spin pumping in $\text{Co}_{20}\text{Fe}_{60}\text{B}_{20}/\text{Pt}$ systems

M. Belmeguenai, K. Aitoukaci, F. Zighem, M. S. Gabor, T. Petrisor, R. B. Mos, and C. Tiusan

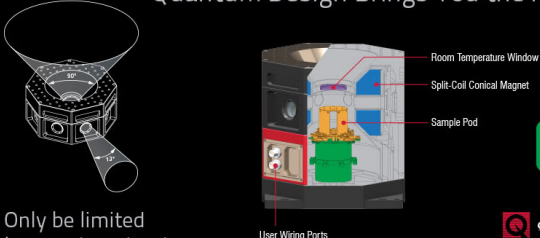
Citation: *Journal of Applied Physics* **123**, 113905 (2018); doi: 10.1063/1.5011111

View online: <https://doi.org/10.1063/1.5011111>

View Table of Contents: <http://aip.scitation.org/toc/jap/123/11>

Published by the *American Institute of Physics*

Quantum Design Brings You the Next Generation Magneto-Optic Cryostat




Only be limited by your imagination...

[Learn More](#)

Quantum Design
qdusa.com/opticool5

8 Optical Access Ports: 7 Side; 1 Top
Temperature Range: 1.7 K to 350 K
7 T Split-Coil Conical Magnet
Low Vibration: <10 nm peak-to-peak
89 mm x 84 mm Sample Volume
Automated Temperature & Magnet Control
Cryogen Free



Investigation of the annealing temperature dependence of the spin pumping in $\text{Co}_{20}\text{Fe}_{60}\text{B}_{20}/\text{Pt}$ systems

M. Belmeguenai,^{1,a)} K. Aitoukaci,¹ F. Zighem,¹ M. S. Gabor,^{2,b)} T. Petrisor, Jr.,² R. B. Mos,² and C. Tiusan^{2,3}

¹LSPM (CNRS-UPR 3407), Université Paris 13, 99 Avenue Jean-Baptiste Clément, 93430 Villetaneuse, France

²Center for Superconductivity, Spintronics and Surface Science, Technical University of Cluj-Napoca, Str. Memorandumului No. 28, RO-400114 Cluj-Napoca, Romania

³Institut Jean Lamour, CNRS, Université de Nancy, BP 70239, F-54506 Vandœuvre, France

(Received 30 October 2017; accepted 1 March 2018; published online 20 March 2018)

$\text{Co}_{20}\text{Fe}_{60}\text{B}_{20}/\text{Pt}$ systems with variable thicknesses of $\text{Co}_{20}\text{Fe}_{60}\text{B}_{20}$ and of Pt have been sputtered and then annealed at various temperatures (T_a) up to 300 °C. Microstrip line ferromagnetic resonance (MS-FMR) has been used to investigate $\text{Co}_{20}\text{Fe}_{60}\text{B}_{20}$ and Pt thickness dependencies of the magnetic damping enhancement due to the spin pumping. Using diffusion and ballistic models for spin pumping, the spin mixing conductance and the spin diffusion length have been deduced from the $\text{Co}_{20}\text{Fe}_{60}\text{B}_{20}$ and the Pt thickness dependencies of the Gilbert damping parameter α of the $\text{Co}_{20}\text{Fe}_{60}\text{B}_{20}/\text{Pt}$ heterostructures, respectively. Within the ballistic simple model, both the spin mixing conductance at the CoFeB/Pt interface and the spin-diffusion length of Pt increase with the increasing annealing temperature and show a strong enhancement at 300 °C annealing temperature. In contrast, the spin mixing conductance, which increases with T_a , shows a different trend to the spin diffusion length when using the diffusion model. Moreover, MS-FMR measurements revealed that the effective magnetization varies linearly with the $\text{Co}_{20}\text{Fe}_{60}\text{B}_{20}$ inverse thickness due to the perpendicular interface anisotropy, which is found to decrease as the annealing temperature increases. It also revealed that the angular dependence of the resonance field is governed by small uniaxial anisotropy which is found to vary linearly with the $\text{Co}_{20}\text{Fe}_{60}\text{B}_{20}$ inverse thickness of the annealed films, in contrast to that of the as grown ones. *Published by AIP Publishing.* <https://doi.org/10.1063/1.5011111>

I. INTRODUCTION

Nowadays, several phenomena are known to occur especially in heavy metal/ferromagnet (FM) systems such as the spin Hall effect (SHE),^{1,2} spin orbit torques,³ the Dzyaloshinskii-Moriya interaction,^{4,5} and the spin pumping.^{6,7} The latter mechanism is considered to be an efficient route to generate a spin current in non-magnetic materials (NMs), which is one of the pillars of modern spintronics.⁸ Ferromagnetic resonance (FMR) induced spin pumping is an emerging process for dynamically injecting a pure spin current into a NM without the need of charge flowing, in contrast to SHE. This involves significant potential impact on the energy efficiency of the spintronic devices. In this process, the resonant precession of the FM magnetization pumps a spin current into the NM, which decays on a length scale called the spin-diffusion length (λ_{SD}). The value of this latter quantity is of great interest, since it could allow the increase of the spin current injection efficiency in the FM/NM bilayer by the optimization of the NM thickness.⁹ The spin injection process into the NM is accompanied by an angular momentum loss in the FM leading to a broadening of the FMR linewidth, which is directly linked to the Gilbert damping parameter (α). The linewidth broadening is more pronounced when the NM is a heavy metal having a high spin-orbit coupling (SOC), due to the increased rate of spin scattering events, owing to the SOC.

This opens an interesting possibility to tune the damping value depending on the desired technological application.

From another side, ferromagnetic CoFeB alloys have attracted an intense attention due to their high spin polarization and low damping properties.^{10–12} Today, CoFeB thin films are considered to be among the most promising candidates for magnetic tunnel junction (MTJ) electrodes due to their ability to provide very large magnetoresistance ratios at room temperature (RT), in conjunction with crystalline MgO tunnel barriers.^{13,14} The CoFeB/MgO based MTJs are widely used in spintronic devices such as magnetic random access memories (MRAMs), magnetic read heads, and magnetic sensors.^{15,16} It is worth mentioning that, unlike the thickness range of CoFeB investigated in this paper, ultrathin CoFeB-based MTJs with a perpendicular magnetic anisotropy due to the interfacial contribution are highly needed for spin transfer torque MRAMs.¹⁷ The magnetic properties of the CoFeB thin films are strongly influenced by their thickness and interfacial effects. It is well known that the room temperature deposited CoFeB films are amorphous and in order to induce their crystallization, an annealing process is required. Therefore, it is of great interest for both fundamental and technological reasons to point out the annealing temperature dependencies of the interfacial anisotropy, the spin diffusion length, and the spin pumping efficiency in $\text{Co}_{20}\text{Fe}_{60}\text{B}_{20}/\text{Pt}$ systems. The experimental strategy used in this paper consists thus to use the ferromagnetic resonance in microstrip line (MS-FMR) under in-plane and perpendicular applied

^{a)}belmeguenai.mohamed@univ-paris13.fr

^{b)}mihai.gabor@phys.utcluj.ro

magnetic fields combined with the vibrating sample magnetometry technique. By investigating the Gilbert damping parameter dependence as a function of the thickness of the $\text{Co}_{20}\text{Fe}_{60}\text{B}_{20}$ and the Pt layers, the spin mixing conductance and λ_{SD} in $\text{Co}_{20}\text{Fe}_{60}\text{B}_{20}/\text{Pt}$ heterostructures have been studied as a function of the annealing temperature. We demonstrate that spin mixing conductance is drastically enhanced for samples annealed at 300°C . Moreover, this work shows the presence of a perpendicular surface magnetic anisotropy, which decreases as the annealing temperature increases.

II. SAMPLE PREPARATION AND EXPERIMENTAL METHODS

$\text{Co}_{20}\text{Fe}_{60}\text{B}_{20}/\text{Pt}$ bilayers were grown at room temperature (RT) onto thermally oxidized Si substrates using a magnetron sputtering system having a base pressure lower than 2×10^{-8} Torr. Two sets of samples have been considered: (i) $\text{Co}_{20}\text{Fe}_{60}\text{B}_{20}$ films with variable thicknesses ($t_{CFB} = 10, 8, 6, 4,$ and 3 nm) capped by a 10 nm thick Pt layer and (ii) 4 nm thick $\text{Co}_{20}\text{Fe}_{60}\text{B}_{20}$ capped by a Pt layer of various thicknesses ($t_{Pt} = 1, 2, 3, 4, 6, 8, 10,$ and 12 nm). After the growth of the stack, the structures were *ex situ* annealed at different temperatures ($T_a = \text{RT}, 200^\circ\text{C}, 250^\circ\text{C},$ and 300°C) for 60 min in vacuum (with a pressure lower than 2×10^{-6} Torr). The first (second) set of samples serves for determining the spin mixing conductance (spin diffusion length) from the investigation of the Gilbert damping parameter of FM/NM heterostructures versus t_{CFB} (versus t_{Pt}). The structural properties of the samples have been determined by x-ray diffraction (XRD) experiments using a four-circle diffractometer. The static magnetic characteristics were investigated by using a vibrating sample magnetometer (VSM). For the dynamic measurements, we used the microstrip ferromagnetic resonance (MS-FMR)¹⁸ technique (in the sweep-field mode), where the external applied magnetic field (up to 1.9 T) is modulated at 170 Hz by a small (4 Oe) alternating magnetic field and the measured signal is proportional to the field first derivative of the absorbed power. During the measurement, the external magnetic field H was applied perpendicular to the sample plane or in-plane in various directions with respect to the sample edges. All the measurements presented here have been performed at room temperature.

III. RESULTS AND DISCUSSIONS

Figure 1 shows the x-ray 2θ - ω (out of plane) diffraction patterns for the CoFeB (6 nm)/Pt (10 nm) measured in a 2θ angle window around the expected positions of the (111) reflection of Pt and the (110) reflection of CoFeB . The patterns show only the (111) Pt diffraction peaks. Laue oscillations are also observable which indicate a good crystalline quality for the Pt films. It should be mentioned that patterns measured on a wider 2θ range did not show the presence of other reflections except for the substrate ones. This indicates that in our samples, Pt has a strong (111) out-of-plane texturing and that the CoFeB films are most likely amorphous or nano-crystalline. This has also been suggested by the lack of a clear in-plane magnetocrystalline anisotropy, confirmed by the VSM measurements. The hysteresis loops for applied

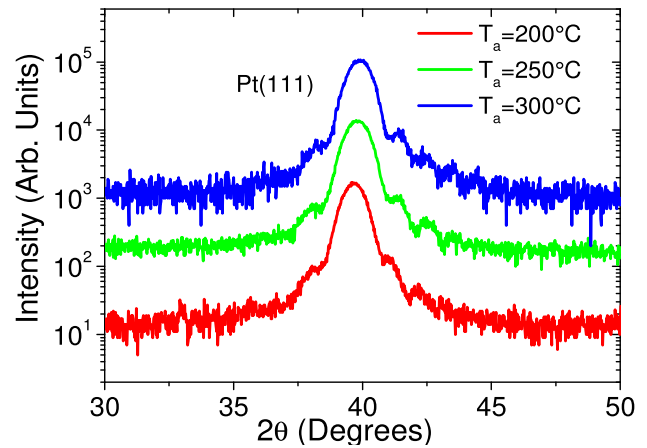


FIG. 1. X-ray 2θ - ω (out of plane) diffraction patterns for $\text{Co}_{20}\text{Fe}_{60}\text{B}_{20}(6\text{nm})/\text{Pt}(10\text{nm})$ thin films annealed at various temperatures.

magnetic fields at various orientations with respect to the substrate edges are illustrated in Fig. 2(a) for CoFeB (4 nm)/Pt (4 nm), indicating a slightly in-plane uniaxial character of the magnetic anisotropy. To test this, we have performed angular remanence magnetization (ARM) measurements, by measuring the remanence magnetization after saturation at different in-plane angles. Figure 2(b) shows the typical normalized ARM curve in our samples presented here for the CoFeB (6 nm)/Pt(10 nm) annealed at 300°C . The shape of the ARM curve is not perfectly isotropic confirming the uniaxial character. This uniaxial character is not surprising for sputtered films, and it is due to the presence of a residual magnetic field of the magnetron sputter sources during growth¹⁹ and it is not connected with in-plane crystalline anisotropy. It is worth mentioning that it was shown that the crystallization of CoFeB and the annealing temperature for which the crystallization occurs are capping material dependent,^{20,21} for instance, $\text{Co}_{40}\text{Fe}_{40}\text{B}_{20}$ crystallization occurs at an annealing temperature of 375°C when MgO is used as the capping layer.²² This suggests that in the case of our Pt capped CoFeB films, higher annealing temperatures are required in order to achieve crystallization.

The magnetization at saturation should be precisely evaluated in order to determine the spin mixing conductance. For this, the thickness dependence of the saturation magnetic moment per unit area has been measured by VSM [shown in Fig. 2(c) only for the as grown and 300°C annealed CoFeB films capped by the 10 nm thick Pt layer, for clarity] and then used to determine the magnetization at saturation and the magnetic dead layer: the slope gives the magnetization at saturation (M_s), while the horizontal axis intercept gives the extent of the magnetic dead layer. As indicated in Fig. 2(c), the magnetic dead layer thickness is nearly zero for these systems whatever the annealing temperature. The magnetization at saturation is determined to be 960 ± 50 , 970 ± 50 , 990 ± 50 , and 1070 ± 70 emu/cm^3 . Within the error bars, it shows a slight increase for the samples annealed at 300°C . For as grown films, the obtained value of the magnetization at saturation is lower than that ($M_s \approx 1200$ emu/cm^3) of $\text{W}/\text{CoFeB}/\text{MgO}$ ²³ and that ($M_s = 1100$ emu/cm^3) of $\text{Ru}/\text{CoFeB}/\text{Ta}$ and $\text{MgO}/\text{CoFeB}/\text{Ta}$.²⁴ However, it is also comparable to the one ($M_s = 800$ – 1100 emu/cm^3) obtained by

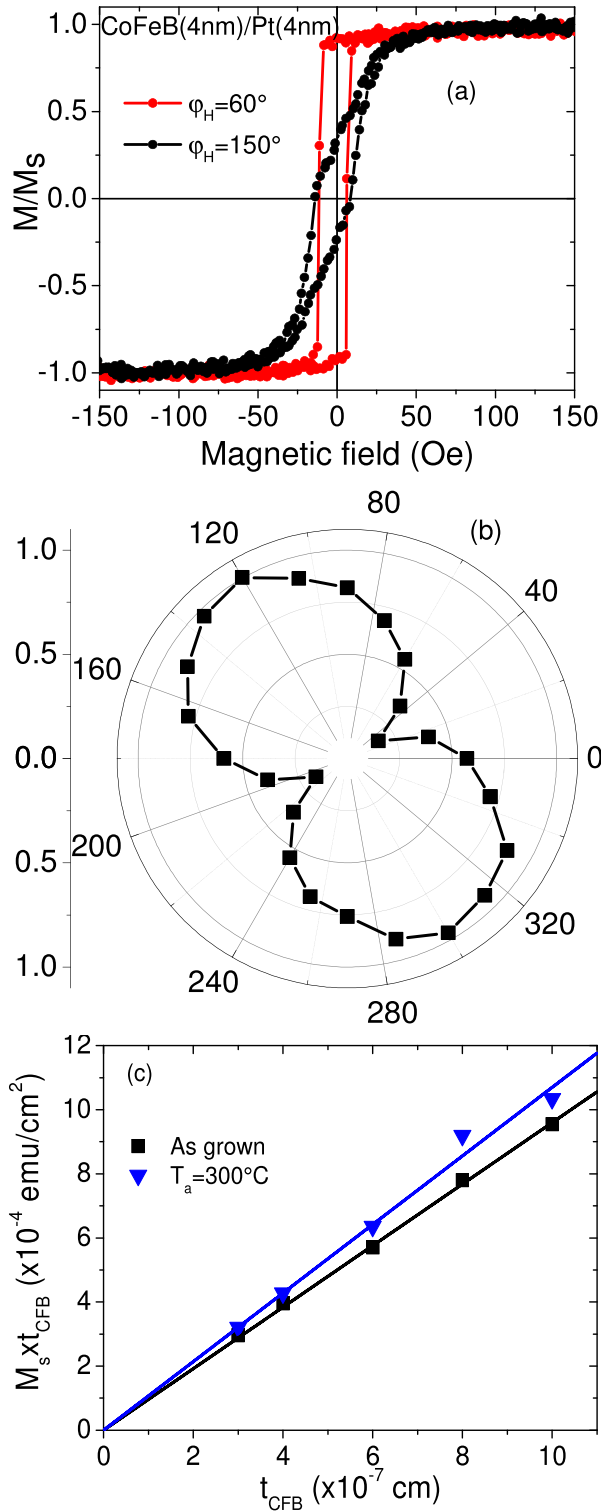


FIG. 2. VSM hysteresis loops of the as grown Co₂₀Fe₆₀B₂₀(4 nm)/Pt(4 nm) measured for an in-plane magnetic field applied at an angle ϕ_H with respect to the substrate edge. (b) Polar representation of the angular remanence curve (ARM) for the Co₂₀Fe₆₀B₂₀(6 nm)/Pt(10 nm) sample annealed at 300 °C showing a weak uniaxial character. (c) Thickness dependencies of the saturation magnetic moment per unit area for the as grown and the 300 °C annealed CoFeB films of various thicknesses (t_{CFB}) capped by the 10 nm thick Pt layer. Symbols in (c) refer to experimental data, and solid lines are linear fits.

Wang et al.²⁵ for Ru/CoFeB/Ru and Ta/CoFeB/Ta. Similar comments can be made for the annealed films at 300 °C. Therefore, we conclude on the possibility of absence/weak

proximity induced magnetization (PIM) in Pt. Since the magnetization of the thin film strongly depends on its interfaces and crystallization degrees of CoFeB, the M_s enhancement with annealing could be attributed to the crystallization of CoFeB at higher annealing temperature. However, since no XRD peaks have been detected for CoFeB films, the increase in M_s is most likely attributed to the boron diffusion away from CoFeB towards the interfaces, which can trigger a transition to a nano-crystalline state and therefore increase the magnetic moment.^{22,26} It is worth mentioning that it is very difficult to have a clear and detectable XRD signal from the nano-crystalline film with very small grain sizes.

The MS-FMR spectra display a single line, identified with the uniform precession mode. The typical obtained MS-FMR spectra are represented in Fig. 3(a) for the as grown 6 nm thick CoFeB layer capped by a 10 nm thick Pt layer under an in-plane applied magnetic field. Due to the static magnetic field modulation (allowing lock-in detection to enhance the measured signal), the recorded signal is thus proportional to the field derivative of the absorption power as a function of the applied magnetic field. However, due to

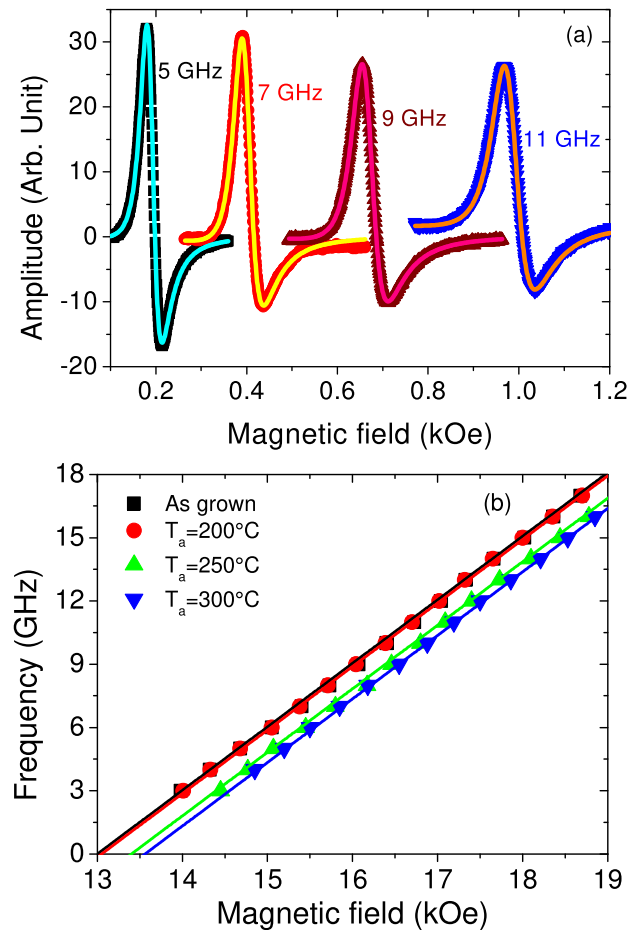


FIG. 3. (a) Ferromagnetic resonance spectra representing the amplitude of the field derivative of the absorbed power as a function of the applied magnetic field for the as grown 6 nm thick CoFeB film capped by a 10 nm thick Pt layer, measured at different driven frequencies. The symbols refer to experimental data and the solid lines are fits using Eq. (1). (b) Variation of the uniform precession mode frequency as a function of the perpendicularly applied magnetic field for Co₂₀Fe₆₀B₂₀(6 nm)/Pt(10 nm) heterostructures annealed at various temperatures T_a . The symbols refer to experimental data and the solid lines are fits using Eq. (2).

the coupling between the magnetic layer and the microstrip line, the recorded spectra are a mixture of dissipative (symmetric) and dispersive parts (as obvious from the asymmetric line shape) of the susceptibility. Therefore, the resonance field and the FMR linewidth of this mode are obtained from the best fit of the recorded data assuming a line shape given by Eq. (1), as shown in Fig. 3(a)

$$\frac{dP_{ab}}{dH} = A_0 \frac{-2\Delta H(H - H_R)\cos(\delta) + [\Delta H^2 - (H - H_R)^2]\sin(\delta)}{[\Delta H^2 + (H - H_R)^2]^2} + A_1, \quad (1)$$

where δ denotes the mixing angle between the dispersive and the dissipative components, A_0 is the amplitude, A_1 is an offset value, H_R is the resonance field, and ΔH is the half linewidth at half maximum. Note that the fitted experimental data with Eq. (1) allows deducing ΔH . However, since the field derivative of the asymmetric absorption signal, which has two peaks [as shown in Fig. 3(a)], is measured, an alternative definition of the linewidth, namely the peak to peak linewidth (ΔH^{PP}) is used. The two linewidths are linked by $\Delta H^{PP} = \frac{2}{\sqrt{3}}\Delta H$. Therefore, in this paper, only ΔH^{PP} , determined using the above-mentioned method, is presented.

The g value, which determines the gyromagnetic factor γ is of utmost important in this study since it is involved in the precise determination of the Gilbert damping and the effective magnetization. It is precisely accessible by the MS-FMR technique through the study of the frequency variation versus the amplitude of the applied magnetic field perpendicular to the film plane. The typical variations of the resonance frequency versus the perpendicular applied magnetic field are shown in Fig. 3(b) for 6 nm thick CoFeB films annealed at various temperatures T_a . Owing to the theoretical variations of the resonance frequency versus the normal to the film plane applied magnetic field given by Eq. (2), the best fits of the experimental data lead to $\gamma/2\pi = 30.13$ GHz/T ($g = 2.15$), which does not show any significant variation versus T_a . This value is in good agreement with that obtained by Devolder¹² for the as deposited films

$$F_{\perp} = \left(\frac{\gamma}{2\pi}\right)(H - 4\pi M_{eff}), \quad (2)$$

where $4\pi M_{eff} = 4\pi M_s - H_{\perp}$ ¹⁷ refers to the effective magnetization and H_{\perp} is the perpendicular anisotropy field. In the above expression, the small in-plane anisotropy fields (less than 50 Oe as it will be shown below) have been neglected, since the applied magnetic fields overpass the 9 kOe in the investigated frequency range, as shown in Fig. 3(b).

Figure 4(a) shows the angular dependencies of the resonance field of the different CoFeB thin films capped by a 10 nm thick Pt layer and annealed at 300°C. It shows that the angular behavior is governed by a small uniaxial anisotropy with the magnetization easy axis direction depending on the sample. To quantify the uniaxial anisotropy field (H_u), the angular dependence, shown in Fig. 4(a), has been analyzed using Eq. (3), giving the resonance frequency for

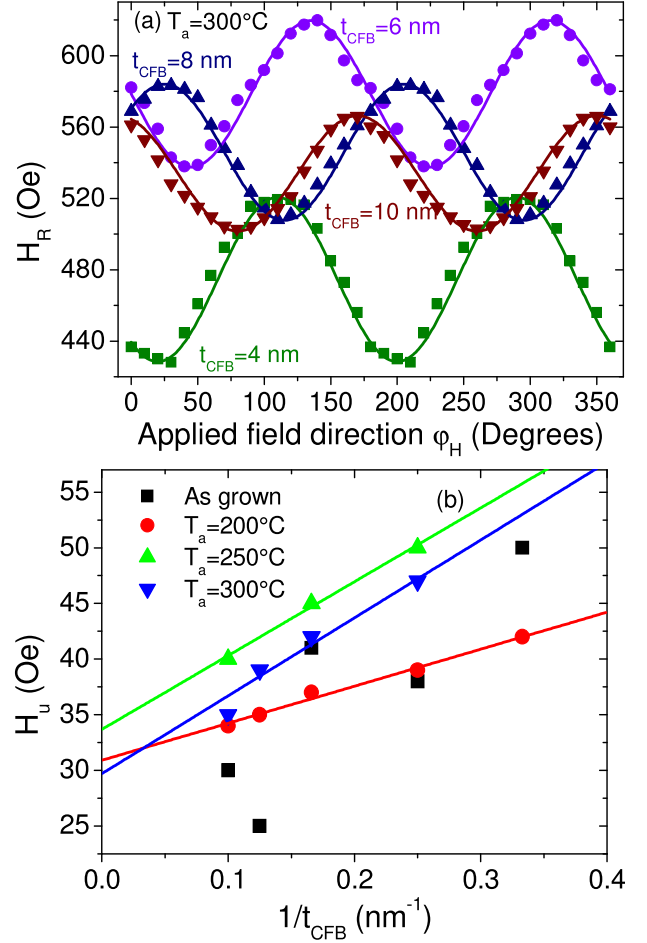


FIG. 4. (a) Resonance field versus the direction of the in-plane applied field with respect to the sample edge (φ_H) measured at 8 GHz driving frequency for $\text{Co}_{20}\text{Fe}_{60}\text{B}_{20}(t_{\text{CFB}})/\text{Pt}(10\text{nm})$ annealed at 300°C. (b) CoFeB thickness (t_{CFB}) dependence of the uniaxial in-plane anisotropy fields (H_u) deduced the angular dependence of the resonance fields of $\text{Co}_{20}\text{Fe}_{60}\text{B}_{20}(t_{\text{CFB}})/\text{Pt}(10\text{nm})$ annealed at various temperatures. The symbols refer to experimental data, and the solid lines are the linear fits.

the in-plane applied magnetic field at an angle φ_H with respect to the sample edges¹⁸

$$F_{//}^2 = \left(\frac{\gamma}{2\pi}\right)^2 [H \cos(\varphi_H - \varphi_M) + H_u \cos 2(\varphi_M - \varphi_u)] \times \left[H \cos(\varphi_H - \varphi_M) + 4\pi M_{eff} + \frac{H_u}{2}(1 + \cos 2(\varphi_M - \varphi_u)) \right], \quad (3)$$

where φ_M (φ_H) and φ_u are angles defining the direction of the magnetization (the applied field) and the planar uniaxial anisotropy easy axis with respect to the substrate edges, respectively.

The variations of H_u versus the inverse CoFeB thickness ($1/t_{\text{CFB}}$) are shown in Fig. 4(b). While H_u of the as grown film does not show a clear behavior versus the CoFeB inverse thickness, clear linear behavior versus $1/t_{\text{CFB}}$ can be observed for the annealed samples as T_a increases, suggesting an interfacial contribution to this the uniaxial anisotropy. The derived uniaxial surface anisotropy constants are 1.6×10^{-3} ,

3.3×10^{-3} , and 3.7×10^{-3} erg/cm², for the 200 °C, 250 °C, and 300 °C annealed films, while the volume uniaxial anisotropy field is around 30 Oe. The precise origin of this interface uniaxial anisotropy is not clear and a completely satisfactory interpretation of H_u and of its T_a dependence is still missing.

The variation of the uniform precession mode resonance frequency has been measured versus the in-plane magnetic field applied along the easy axis and then fitted using Eq. (3) to extract the effective magnetization for each sample. Figure 5(a) shows the extracted effective magnetization versus the inverse film thickness $1/t_{CFB}$ for the various annealing temperatures. It can be seen that M_{eff} follows a linear variation. We conclude that the perpendicular anisotropy field includes a surface energy term. Therefore, the effective perpendicular anisotropy constant K_{\perp} (with $H_{\perp} = 2K_{\perp}/M_s$) could be phenomenologically separated in a volume and an interface contributions and approximately obeys the relation $K_{\perp} = K_v + K_s/t_{CFB}$.^{27–29} This allows us to derive the perpendicular surface anisotropy constants $K_s = 1.33$, 1.11, 0.97, and 0.74 erg/cm², respectively, for $T_a = RT$, 200 °C, 250 °C, and 300 °C. Similarly, the deduced perpendicular volume constants are found to be $K_v = -2.12 \times 10^6$, -1.81×10^6 ,

-1.52×10^6 , and -0.52×10^6 erg/cm³, respectively, for $T_a = RT$, 200 °C, 250 °C, and 300 °C. Both anisotropy constants decrease with increasing annealing temperature. Several explanations can be given for the origin of this linear behavior of the effective magnetization versus the CoFeB thickness and its dependence on T_a : (i) magneto-elastic anisotropy contribution, (ii) roughness that creates in-plane demagnetizing fields at the edges of terraces reducing the shape anisotropy and therefore, favors perpendicular magnetization, and (iii) interdiffusion and mixing which might occur at the interfaces during the deposition of the layers introducing thus, randomness in the magnetic pair bonds accordingly, which obviously reduces the interface anisotropy.²⁹ (iv) Another possible reason for the perpendicular magnetic anisotropy is the interfacial hybridization between the magnetic and the Pt metals. These four mechanisms are annealing temperature dependent. Although, mixing at the interface should be excluded since no magnetic dead layer has been revealed from the VSM measurement and in contrast intermixing of Co (or Fe) with Pt forms CoPt or FePt alloys which are well-known to have perpendicular anisotropy (increase in anisotropy constants), it is not again obvious to determine which mechanism is responsible of this interface anisotropy. Moreover, according to Ref. 29, the influence of the misfit strain appears as a volume contribution to the anisotropy and can lead to an apparent interface contribution for ultrathin films below some critical thickness (around 3 nm). It is thus most likely that the electron hybridization plays the most important role in dictating this interface magnetic anisotropy. The variation of M_{eff} versus the capping Pt layer thickness is shown in Fig. 5(b) for the 4 nm thick CoFeB films. While it fluctuates slightly for the as grown and films annealed at 200 °C, significant changes can be observed for films annealed at 300 °C, where significant interface changes occur. Its mean value increases with increasing T_a confirming the decrease of perpendicular anisotropy.

The field peak to peak linewidth (ΔH^{PP}) has been obtained from the fit [using Eq. (1)] of MS-FMR spectra measured under an in-plane applied field at various directions with respect to the substrate edges. Since the presence of extrinsic contributions³⁰ to FMR linewidth, which are usually field direction dependent (anisotropic), lead to an overestimation of Gilbert damping, the angular dependence of ΔH^{PP} has been measured for each sample. The direction giving the minimal ΔH^{PP} value and thus minimizing the extrinsic contributions to the linewidth has thus been determined. This in-plane direction is found to be sample dependent similar to the direction of the in-plane anisotropy easy axis. The frequency dependencies of this linewidth have then been measured for the magnetic field applied along this direction as shown in Fig. 6(a) for CoFeB(6 nm)/Pt(10 nm) annealed at various temperatures. It is clearly seen for all samples that ΔH^{PP} varies linearly with frequency, leading to the conclusion that the damping is Gilbert type and not caused by any other processes. Therefore, the used measurement scheme, consisting of determining the direction of the applied field giving the minimal value of ΔH^{PP} , seems to be efficient to avoid any extrinsic contributions to damping since extrinsic contributions to damping should lead to non-linear variation for

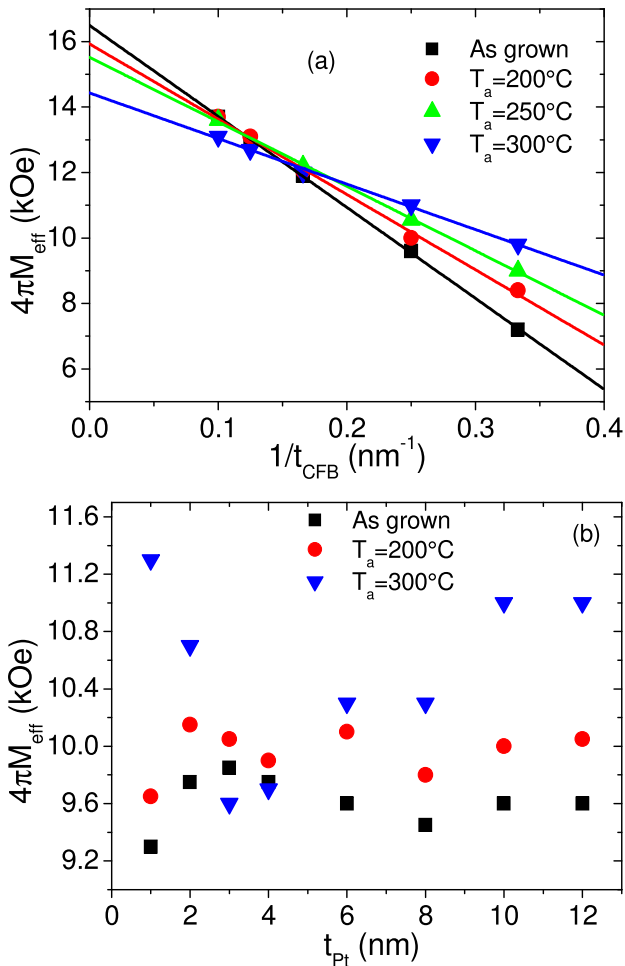


FIG. 5. (a) CoFeB thickness dependence of the effective magnetization ($4\pi M_{eff}$) extracted from the fit of FMR measurements for CoFeB thin films of thickness t_{CFB} capped with a 10 nm thick Pt layer and annealed at T_a . The symbols refer to experimental data, and the solid lines are linear fits. Pt thickness dependence of $4\pi M_{eff}$ for CoFeB(4 nm)/Pt(t_{Pt}) films annealed at T_a .

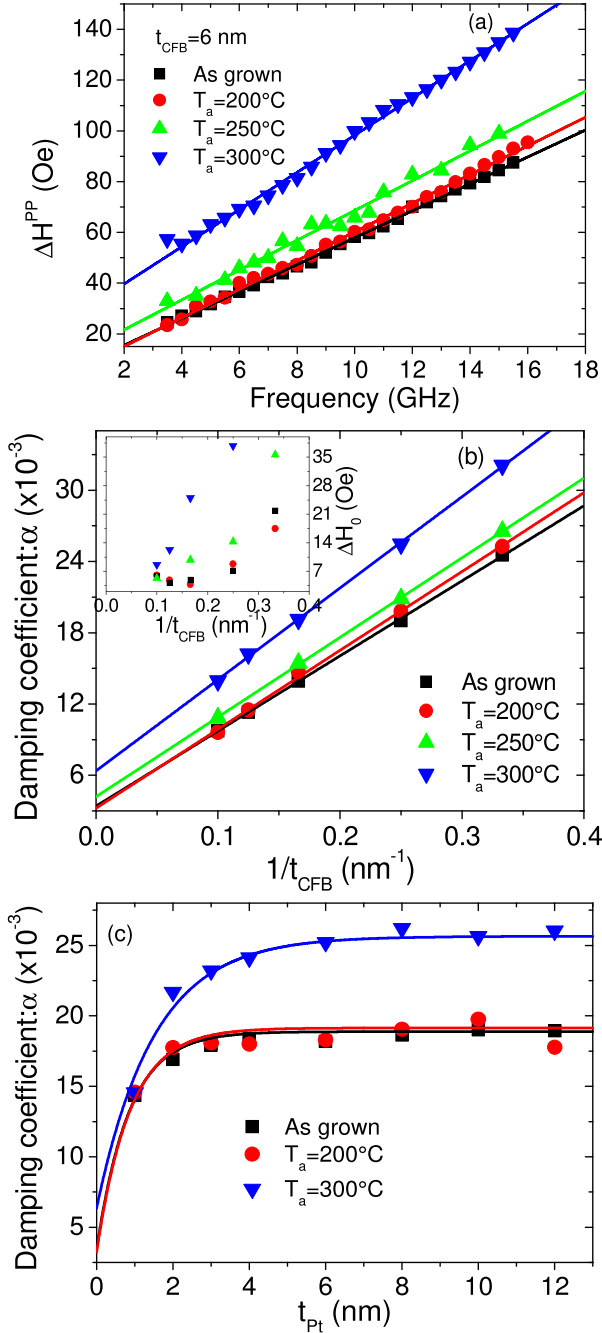


FIG. 6. (a) Peak to peak FMR field linewidth versus the driven frequency measured for the magnetic field applied in the direction where ΔH^{PP} is minimal and (b) CoFeB thickness dependence of the Gilbert damping parameter, deduced from the frequency dependence of the linewidth using Eq. (4), of the CoFeB thin films of a thickness t_{CFB} capped by a 10 nm Pt layer and annealed at different temperatures. The inset shows the evolution of the inhomogeneous FMR linewidth versus the CoFeB thickness for various T_a . (c) Pt thickness dependence of the Gilbert damping parameter, deduced from the frequency dependence of the linewidth using Eq. (4), of the 4 nm thick CoFeB thin films capped with the Pt layer of thickness (t_{Pt}) and annealed at different temperatures. The symbols refer to experimental data, and the solid lines in (b) and (c) are fits using the ballistic model described in the paper and the parameters summarized in Table I.

ΔH^{PP} . Moreover, as we mentioned above, the uniaxial anisotropy fields in our samples are very weak. Therefore, these fields are very low compared to the resonance fields at the driven frequencies used in this work (3–18 GHz). Indeed, in this condition, the magnetization direction will be almost

parallel to the applied magnetic field ($\varphi_M = \varphi_M$). Therefore, experimental data of the frequency dependence of ΔH^{PP} have been fitted using the simple equation (4) leading to the determination of the damping parameter α ^{30,31}

$$\Delta H^{PP} = \Delta H_0 + \frac{2}{\sqrt{3}} \frac{\alpha}{\gamma} 2\pi f, \quad (4)$$

where f is the driven frequency and ΔH_0 is the inhomogeneous residual peak to peak linewidth, which is frequency independent. The multiplying factor of $\frac{1}{\sqrt{3}}$, in Eq. (4), is the correction of the difference between the full width at half maximum (FWHM) and the peak to peak linewidth for the line shape of Lorentzian.³¹

The obtained results from the fit of experimental data, using Eq. (4), are shown in Figs. 6(b) and 6(c) as a function of the CoFeB and the Pt thicknesses, respectively. Figure 6(b) reveals that the damping constant increases linearly with $1/(t_{CFB})$. The dependence of α versus the Pt thickness, presented in Fig. 6(c) for the 4 nm thick CoFeB layer, shows an exponential behavior. Due to the linear variation of ΔH^{PP} versus the frequency (Gilbert type damping) and since the extrinsic contributions to damping have been minimized, the enhancement of the damping as t_{CFB} decreases and its dependence on Pt thickness are attributed to the spin pumping current induced in Pt by the FMR precession of magnetization. In fact, according to the theory,³² if this additional damping ($\Delta\alpha$) is caused by spin pumping, then the FMR linewidth which contains $\alpha_{CFB} + \Delta\alpha$ (where α_{CFB} is the intrinsic Gilbert damping constant of CoFeB), should vary linearly versus the microwave frequency as shown in Fig. 6(a). This amount of the spin pumping is closely related to the SOC through the spin flip relaxation time and the spin mixing conductance that we aim to determine below. Moreover, it should be mentioned that the inhomogeneity contribution to the linewidth broadening ΔH_0 decreases as the CoFeB thickness increases and it increases with the annealing temperature as shown in the inset of Fig. 6(b): a linear dependence versus $1/t_{CFB}$, suggesting an interface contribution, can be observed.

To analyze this behavior of damping, we will consider two models (ballistic and diffusive models). Both models consider that the net spin current (I^s) through the interface FM/NM is given by $I^s = I^{pump} - I^{back}$, where I^{pump} and I^{back} are the spin pumped and the backflow spin currents, respectively, but differ in the evaluation of I^{back} . In the ballistic limit,³³ λ_{SD} is much lower than the mean free path of electrons. Therefore, the NM is considered as a perfect conductor and thus the I^{back} varies exponentially with the NM thickness.³³ Within this simple model, the thickness dependencies of the total damping are given by Eqs. (5)^{33,34} and (6)^{33,35}

$$\alpha = \alpha_{CFB} + \frac{g\mu_B}{4\pi M_s t_{CFB}} g^{\uparrow\downarrow}, \quad (5)$$

$$\alpha = \alpha_{CFB} + \frac{g\mu_B}{4\pi M_s t_{CFB}} g^{\uparrow\downarrow} \left[1 - e^{-\frac{2t_{Pt}}{\lambda_{SD}}} \right], \quad (6)$$

where μ_B is the Bohr magneton and $g^{\uparrow\downarrow}$ is the intrinsic spin mixing conductance of the interface CoFeB/Pt. Note that Eq. (5) is only valid for thick enough NM layers with respect

to λ_{SD} , where no reflection of the spin current takes place at interfaces. It can thus be obtained from Eq. (6), which has been obtained by assuming that λ_{SD} is much lower than the mean free path of electrons and considering that the backflow spin current varies exponentially with the NM thickness. By fitting experimental data of Fig. 6 with Eqs. (5) and (6), the determined values of α_{CFB} , λ_{SD} , and $g^{\uparrow\downarrow}$ are summarized in Table I. The intrinsic damping of the CoFeB increases with the annealing temperature similar to the reported behavior by Conca *et al.*²² and by Bilzer *et al.*³⁶ The increase in α_{CFB} with increasing annealing temperature could be caused by severe atomic intermixing between the magnetic and the adjacent nonmagnetic layers and/or by the development of polycrystalline grains. However, since no magnetic dead layer has been detected from the VSM measurements, the increase in α_{CFB} is probably due the development of polycrystalline grains after annealing. Note also the enhancement of the spin mixing conductance and spin diffusion length as the annealing temperature increases.

An important phenomenon that accompanies the magnetization precession induced spin injection is the back diffusion (backflow) of injected spins to the interface, which effectively reduces the spin current injection. This backflow current has been approximatively modelled within the ballistic approach [Eq. (6)]. Therefore, an alternative model (diffusive model)³⁷ where the spin accumulation at the FM/NM interface, generated by the injected spins, is taken into account when calculating the backflow spin current has been introduced. Within this model, the additional damping due to the spin pumping is given by

$$\Delta\alpha = \frac{g\mu_B}{4\pi M_s t_{CFB}} \frac{g^{\uparrow\downarrow}}{1 + \frac{g^{\uparrow\downarrow}}{g_{ext}}}, \quad (7)$$

where g_{ext} is the electrical conductance of Pt and σ_{Pt} is given by $g_{ext} = \frac{\hbar}{e^2} \frac{\sigma_{Pt}}{\lambda_{SD}} \tanh\left(\frac{t_{Pt}}{\lambda_{SD}}\right)$,³⁷ for a simple FM/NM interface. Note that in contrast to the ballistic model, this model takes into account the finite electrical resistance of the NM material, which depends on the preparation conditions and may include interface contribution. Indeed, if the conductivity of a NM layer is assumed to be constant, but in reality it decreases with the decreasing layer thickness (as we will

TABLE I. Parameters obtained from the best fit of the thickness dependencies of damping of CoFeB/Pt systems annealed at various temperatures using two different models (Ballistic and diffusive), described in the text. n.m. refers to “not measured.”

T_a (°C)	Model	α_{CFB} ($\times 10^{-3}$)	$g^{\uparrow\downarrow}$ (nm^{-2})	λ_{SD} (nm)
RT	Ballistic	3.4	38.6	1.7
	Diffusive	3.4	42.1	0.37
200	Ballistic	3.23	41	1.75
	Diffusive	3.23	45.3	0.37
250	Ballistic	4.2	42.2	n.m
	Diffusive	n.m	n.m	n.m
300	Ballistic	6.4	52.4	3
	Diffusive	6.5	65.5	0.28

show below), and the fitted spin diffusion length will incur a systematic inaccuracy.³⁸ Thus, fits of spin pumping data with a model that ignores the thickness dependence of the conductivity provide, at best, an upper bound.³⁸ Therefore, to analyze the thickness dependence of damping through this model, the sheet resistance (R_{Sheet}) of the entire CoFeB(4 nm)/Pt(t_{Pt}) has been measured as a function of the Pt thickness using a four-probe method with an in-plane current. Figure 7(a) shows the typical behavior for samples annealed at 200 and 300 °C for clarity. By assuming that the CoFeB layer resistivity is constant in CoFeB (4 nm)/Pt(t_{Pt}) and that this CoFeB layer together with the Pt layer act as parallel resistors, the sheet resistance can be written as³⁸

$$R_{Sheet} = \left(\frac{t_{CFB}}{\rho_{CFB}} + \frac{t_{Pt}}{\rho_{Pt}} \right), \quad (8)$$

where ρ_{Pt} , ρ_{CFB} are the Pt and the CoFeB resistivity and $t_{CFB} = 4$ nm is the thickness of the CoFeB layer. The fit of experimental data of Fig. 7(a) with Eq. (8) revealed that the resistivities of Pt scale inversely with its thickness, suggesting an interfacial contribution due to interface scattering of conduction electrons,^{38,39} and allowed to isolate both volume and interface contributions. While the volume resistivity (ρ_v) of Pt is found to be insensitive to the annealing temperature ($\rho_v = 1.7 \times 10^{-7} \Omega \text{m}$ and $\rho_v = 1.8 \times 10^{-7} \Omega \text{m}$ for $T_a = \text{RT}$ and 300 °C, respectively), the interface resistivity (ρ_s) increases drastically with the annealing temperature (for instance, $\rho_s = 9 \times 10^{-16} \Omega \text{m}^2$ and $\rho_s = 16 \times 10^{-16} \Omega \text{m}^2$ for $T_a = \text{RT}$ and 300 °C, respectively), suggesting an enhanced interface scattering of charges, most likely due to B diffusion at the interface. The obtained values of the volume resistivities are similar to the previously reported measured values ($1.6\text{--}2 \times 10^{-7} \Omega \text{m}$).^{38,40,41} We used the function of the thickness dependent of ρ_{Pt} , obtained from the fit of R_{Sheet} measurements, with Eq. (8) to fit the experimental data of both the thickness dependencies of the damping as shown in Figs. 7(b) and 7(c). The fitting parameters are λ_{SD} , $g^{\uparrow\downarrow}$, and α_{CFB} . The obtained values are tabulated in Table I. Apart from the similar values of α_{CFB} , the diffusive model gives higher (lower) values of $g^{\uparrow\downarrow}$ (λ_{SD}) compared to the ballistic model. The higher value of $g^{\uparrow\downarrow}$ in the diffusive model is a consequence of the underestimation of the backflow spin current in the ballistic model. Therefore, to obtain the same net spin current, the spin mixing conductance should be higher for the diffusive model. The similar trend versus the annealing temperature of the obtained values of λ_{SD} and $g^{\uparrow\downarrow}$ using the ballistic model is unexpected. Indeed, the increase in both λ_{SD} and $g^{\uparrow\downarrow}$ is not compatible. Since the increase in the spin mixing conductance implies more losses of the magnetic moment in the NM material, one expects a decrease in the spin diffusion length, in accordance with the behavior of λ_{SD} and $g^{\uparrow\downarrow}$ deduced from fit using the diffusive model. The neglect of the electrical resistivity, especially when it is thickness dependent and of the spin accumulation in the ballistic model could lead to wrong conclusion and interpretation of the obtained results. The use of the spin diffusive model incorporating the thickness dependence of the Pt resistivity leads to an accurate determination of the intrinsic

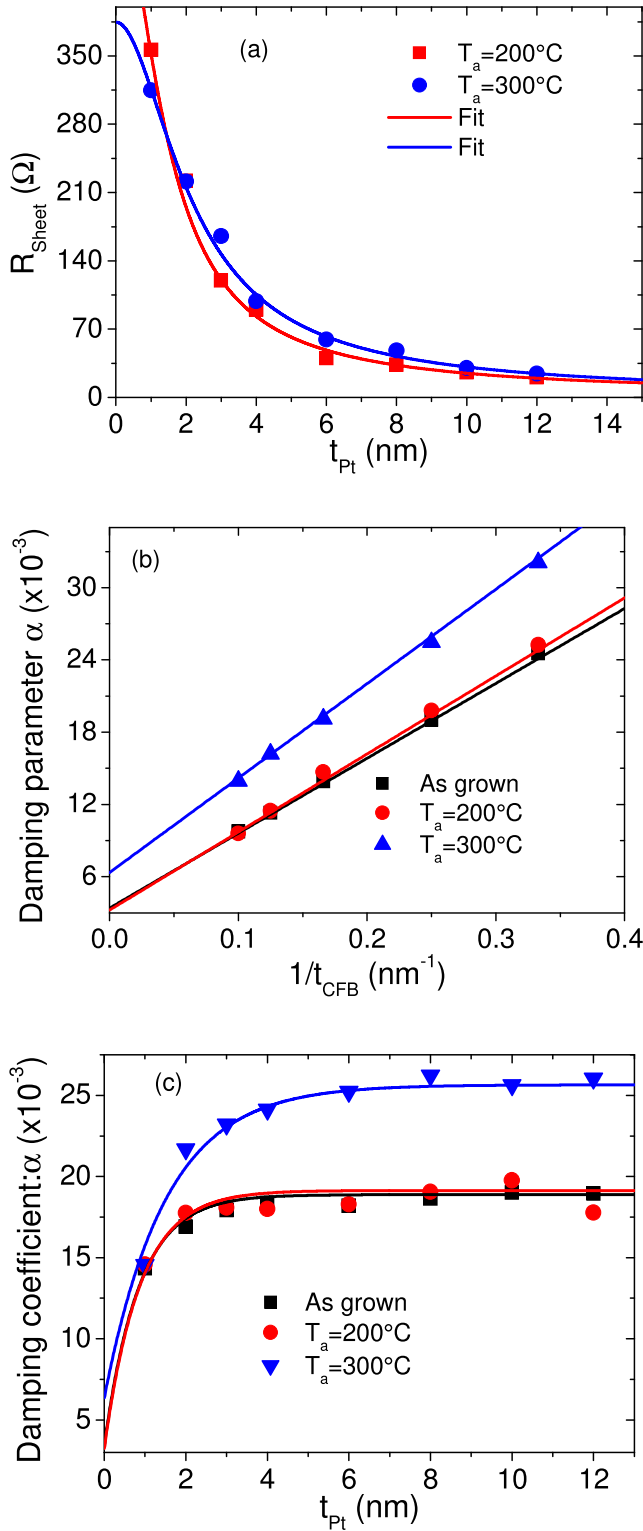


FIG. 7. (a) Pt thickness dependence of the four-probes measured sheet resistance of CoFeB(4 nm)/Pt(t_{Pt}) films annealed at 200 and 300 °C. The symbols refer to the measurements, and the solid lines are fits using Eq. (8). (b) CoFeB thickness dependence of the Gilbert damping parameter, deduced from the frequency dependence of the linewidth using Eq. (4), of CoFeB thin films of thickness t_{CFB} capped by a 10 nm Pt layer and annealed at different temperatures. (c) Pt thickness dependence of the Gilbert damping parameter, deduced from the frequency dependence of the linewidth using Eq. (4), of the 4 nm thick CoFeB thin films capped with the Pt layer of thickness (t_{Pt}) and annealed at different temperatures. The symbols refer to experimental data, and the solid lines in (b) and (c) are fits using the diffusive model described in the paper and the parameters summarized in Table I.

spin-mixing conductance and the spin diffusion length. It is worth mentioning that due to the lack of experimental proof that spin transport can proceed via ballistic channels in metallic multilayer structures even when thicknesses are less than the mean free path,⁴² the diffusive model remains more realistic for experimental data analysis. We should mention that the increase in the intrinsic damping, the intrinsic spin mixing conductance, the surface resistivity of Pt, and the decrease in the spin diffusion length and the perpendicular anisotropy as the annealing temperature increases are coherent and could be linked to the evolution of the CoFeB/Pt interface with annealing. However, the exact reason for this behaviour remains unclear and only speculation can be given. The efficiency of spin current injection across CoFeB/Pt interfaces and thus the spin mixing conductance depends on the crystalline ordering of CoFeB, as well as the smoothness and cleanliness of the interface. In fact, according to first-principles calculation^{43,44} the interface roughness as well as the disorder generally enhances spin mixing conductance and hence the s-d exchange coupling. Surface/interface roughness and disorder in thin films contribute to electron scattering and thus to film electrical resistivity.^{45,46} Therefore, since a drastic increase in the surface contribution to the electric resistivity for samples annealed at 300 °C has been observed, we speculate that the interface roughness and/or disorder increases with the annealing temperature. The enhancement of the spin mixing conductance of the CoFeB/Pt interface with the annealing temperature is thus most probably due to the increase in the disorder and/or interface roughness. This is in good agreement with the observed decrease in the interface anisotropy as the annealing temperature increases. Note the discrepancy of the published values of the spin diffusion length (due to the interface quality and conductivity difference which are growth dependent) for Pt, ranging from 0.5 to 10 nm.³⁸ Lower values have been also obtained³⁸ and therefore, the obtained values here of λ_{SD} using the two models are within this range.

Finally, we should comment on the effect of the proximity induced magnetization on the damping. In FM/Pt systems, it is usually expected that the ferromagnetism may extend beyond the physical structure of the interface and results in proximity induced magnetization (PIM) in Pt. This produces extra damping as it has been observed by Sun *et al.*⁴⁷ in yttrium iron garnet (YIG)/Pt and affects the spin mixing conductance. According to Sun *et al.*, the extra damping originates from the ferromagnetic ordering in Pt atomic layers near the FM/Pt interface and the dynamic exchange coupling between the ordered Pt spins and spins in the FM film.⁴⁷ Indeed, Sun claimed that because of the presence of the ferromagnetic Pt (FM Pt), the conventional spin pumping from the YIG film (in his case) to the Pt film does not occur. However, there exists a spin pumping from the FM Pt into the paramagnetic Pt, which contributes to the damping of the FM Pt. The dynamic YIG-Pt coupling allows for the transfer of a part of the damping of the FM Pt to the YIG film. This extra damping cannot be described by existing models and therefore new theoretical models on damping in FM/NM are needed. This role has been addressed experimentally by Caminale *et al.*⁴⁸ who showed that PIM yields a nearly linear dependence of

the interface-related Gilbert damping enhancement on the heavy metal layer thicknesses for low thickness values (below 2 nm for Pt). In the absence of x-ray resonant magnetic reflectivity measurements (XRMR), we cannot conclude on the absence/presence of PIM in our sample although the lower measured M_s with respect to other systems including CoFeB. Therefore, we cannot estimate the contribution of PIM to spin pumping damping. XRMR combined to MS-FMR measurements will be used in forthcoming papers to address the link between PIM and spin pumping damping.

IV. CONCLUSION

The thickness dependencies of Gilbert damping constant have been used to measure both the spin diffusion length and the spin mixing conductance in CoFeB/Pt systems via the ferromagnetic resonance induced spin pumping. Special interest has been given to the effect of the annealing temperature on damping, spin mixing conductance, spin diffusion length, and magnetic anisotropy. The obtained results on damping demonstrate the efficiency of the possibility of tuning the Gilbert damping constant by a judicious choice of the non-magnetic layer and the annealing temperature, depending on the desired application. The experimental results have been analysed considering diffusive and ballistic models to deal with the additional damping induced by the spin pumping. A comparison between the two models revealed that the diffusive model enhances the accuracy on the determination of spin mixing conductance and spin diffusion length, especially when the electrical resistivity of the NM is thickness dependent. We also showed that the perpendicular anisotropy in CoFeB/Pt systems includes an interface contribution that increases with decreasing annealing temperatures.

ACKNOWLEDGMENTS

This work has been partially supported by the Conseil Régional, Île-de-France through the DIM NanoK (BIDUL project). M.S.G., T.P., and R.B.M. acknowledge the financial support of UEFISCDI through PN-II-RU-TE-2014-4-1820 SPINCOD Research Grant No. 255/01.10.2015.

- ¹Y. K. Kato, R. C. Myers, A. C. Gossard, and D. D. Awschalom, *Science* **306**, 1910 (2004).
- ²J. Wunderlich, B. Kaestner, J. Sinova, and T. Jungwirth, *Phys. Rev. Lett.* **94**, 047204 (2005).
- ³S. Woo, M. Mann, A. J. Tan, L. Caretta, and G. S. D. Beach, *Appl. Phys. Lett.* **105**, 212404 (2014).
- ⁴I. E. Dzyaloshinskii, *Sov. Phys. JETP* **5**, 1259 (1957).
- ⁵T. Moriya, *Phys. Rev.* **120**, 91 (1960).
- ⁶A. Brataas, Y. Tserkovnyak, G. E. W. Bauer, and B. I. Halperin, *Phys. Rev. B* **66**, 060404 (2002).
- ⁷Y. Tserkovnyak, A. Brataas, G. E. W. Bauer, and B. I. Halperin, *Rev. Mod. Phys.* **77**, 1375 (2005).
- ⁸J. Sinova, S. O. Valenzuela, J. Wunderlich, C. H. Back, and T. Jungwirth, *Rev. Mod. Phys.* **87**, 1213 (2015).
- ⁹H. Ulrichs, V. E. Demidov, S. O. Demokritov, W. L. Lim, J. Melander, N. Ebrahim-Zadeh, and S. Urazhdin, *Appl. Phys. Lett.* **102**, 132402 (2013).
- ¹⁰T. Kubota, T. Daibou, M. Oogane, Y. Ando, and T. Miyazaki, *Jpn. J Appl. Phys., Part 2* **46**, L250 (2007).
- ¹¹S. X. Huang, T. Y. Chen, and C. L. Chien, *Appl. Phys. Lett.* **92**, 242509 (2008).
- ¹²T. Devolder, P.-H. Ducrot, J.-P. Adam, I. Barisic, N. Vernier, J.-V. Kim, B. Ockert, and D. Ravelosona, *Appl. Phys. Lett.* **102**, 022407 (2013).
- ¹³S. S. P. Parkin, C. Kaiser, A. Panchula, P. M. Rice, B. Hughes, M. Samant, and S. H. Yang, *Nat. Mater.* **3**, 862 (2004).
- ¹⁴D. D. Djayaprawira, K. Tsunekawa, M. Nagai, H. Maehara, S. Yamagata, N. Watanabe, N. Watanabe, S. Yuasa, Y. Suzuki, and K. Ando, *Appl. Phys. Lett.* **86**, 092502 (2005).
- ¹⁵S. Tehrani, B. Engel, J. M. Slaughter, E. Chen, M. DeHerrera, M. Durlam, P. Naji, R. Whig, J. Janesky, and J. Calder, *IEEE Trans. Magn.* **36**, 2752 (2000).
- ¹⁶J. Lenz and S. Edelstein, *IEEE Sens. J.* **6**, 631 (2006).
- ¹⁷B. Diény and M. Chshiev, *Rev. Mod. Phys.* **89**, 025008 (2017).
- ¹⁸M. Belmeguenai, F. Zighem, Y. Roussigné, S. M. Chérif, P. Moch, K. Westerholt, G. Woltersdorf, and G. Bayreuther, *Phys. Rev. B* **79**, 024419 (2009).
- ¹⁹Y. Lu and A. Nathan, *Appl. Phys. Lett.* **70**, 526 (1997).
- ²⁰T. Ibusuki, T. Miyajima, S. Umehara, S. Eguchi, and M. Sato, *Appl. Phys. Lett.* **94**, 62509 (2009).
- ²¹C. Park, Y.-H. Wang, D. E. Laughlin, and J.-G. Zhu, *IEEE Trans. Magn.* **42**, 2639 (2006).
- ²²A. Conca, E. T. Papaioannou, S. Klingler, J. Greser, T. Sebastian, B. Leven, J. Löscher, and B. Hillebrands, *Appl. Phys. Lett.* **104**, 182407 (2014).
- ²³C.-F. Pai, M.-H. Nguyen, C. Belvin, L. H. Vilela-Leão, D. C. Ralph, and R. A. Buhrman, *Appl. Phys. Lett.* **104**, 082407 (2014).
- ²⁴S. Y. Jang, C.-Y. You, S. H. Lim, and S. R. Lee, *J. Appl. Phys.* **109**, 013901 (2011).
- ²⁵Y.-H. Wang, W.-C. Chen, S.-Y. Yang, K.-H. Shen, C. Park, M.-J. Kao, and M.-J. Tsai, *J. Appl. Phys.* **99**, 08M307 (2006).
- ²⁶T. Dimopoulos, G. Gieres, J. Wecker, N. Wiese, and M. D. Sacher, *J. Appl. Phys.* **96**, 6382 (2004).
- ²⁷S. Ikeda, K. Miura, H. Yamamoto, K. Mizunuma, H. D. Gan, M. Endo, S. Kanai, J. Hayakawa, F. Matsukura, and H. Ohno, *Nature Mater.* **9**, 721 (2010).
- ²⁸A. Kaidatzis, C. Bran, V. Psycharis, M. Vázquez, J. M. García-Martín, and D. Niarchos, *Appl. Phys. Lett.* **106**, 262401 (2015).
- ²⁹M. T. Johnson, P. J. H. Bloemenz, F. J. A. den Broeder, and J. J. de Vries, *Rep. Prog. Phys.* **59**, 1409 (1996).
- ³⁰K. Zakeri, J. Lindner, I. Barsukov, R. Meckenstock, M. Farle, U. von Hörsten, H. Wende, W. Keune, J. Rocker, S. S. Kalarickal, K. Lenz, W. Kuch, K. Baberschke, and Z. Frajt, *Phys. Rev. B* **76**, 104416 (2007).
- ³¹S. Mizukami, Y. Ando, and T. Miyazaki, *Phys. Rev. B* **66**, 104413 (2002).
- ³²Y. Tserkovnyak, A. Brataas, and G. E. W. Bauer, *Phys. Rev. Lett.* **88**, 117601 (2002).
- ³³J. Foros, G. Woltersdorf, B. Heinrich, and A. Brataas, *J. Appl. Phys.* **97**, 10A714 (2005).
- ³⁴M. Tokaç, S. A. Bunyayev, G. N. Kakazei, D. S. Schmool, D. Atkinson, and A. T. Hindmarch, *Phys. Rev. Lett.* **115**, 056601 (2015).
- ³⁵J. M. Shaw, H. T. Nembach, and T. J. Silva, *Phys. Rev. B* **85**, 054412 (2012).
- ³⁶C. Pilzer, T. Devolder, J.-V. Kim, G. Counil, C. Chappert, S. Cardoso, and P. P. Freitas, *J. Appl. Phys.* **100**, 053903 (2006).
- ³⁷Y. Tserkovnyak, A. Brataas, and G. E. W. Bauer, *Phys. Rev. B* **66**, 224403 (2002).
- ³⁸C. T. Boone, J. M. Shaw, H. T. Nembach, and T. J. Silva, *J. Appl. Phys.* **117**, 223910 (2015).
- ³⁹H. D. Liu, Y.-P. Zhao, G. Ramanath, S. P. Murarka, and G.-C. Wang, *Thin Solid Films* **384**(1), 151–156 (2001).
- ⁴⁰L. Vila, T. Kimura, and Y. Otani, *Phys. Rev. Lett.* **99**, 226604 (2007).
- ⁴¹L. Liu, T. Moriyama, D. C. Ralph, and R. A. Buhrman, *Phys. Rev. Lett.* **106**, 036601 (2011).
- ⁴²C. T. Boone, H. T. Nembach, J. M. Shaw, and T. J. Silva, *J. Appl. Phys.* **113**, 153906 (2013).
- ⁴³Q. Zhang, S.-I. Hikino, and S. Yunoki, *Appl. Phys. Lett.* **99**, 172105 (2011).
- ⁴⁴K. Xia, P. J. Kelly, G. E. Bauer, A. Brataas, and I. Turek, *Phys. Rev. B* **65**, 220401 (2002).
- ⁴⁵G. Palasantzas, *Phys. Rev. B* **58**, 9685 (1998).
- ⁴⁶J. S. Agustsson, U. B. Arnalds, A. S. Ingason, K. B. Gylfason, K. Johnsen, S. Olafsson, and J. T. Gudmundsson, *J. Phys.: Conf. Ser.* **100**, 082006 (2008).
- ⁴⁷Y. Sun, H. Chang, M. I. Kabatek, Y.-Y. Song, Z. Wang, M. Jantz, W. Schneider, M. Wu, E. Montoya, B. Kardasz, B. Heinrich, S. G. E. te Velthuis, H. Schultheiss, and A. Hoffmann, *Phys. Rev. Lett.* **111**, 106601 (2013).
- ⁴⁸M. Caminale, A. Ghosh, S. Auffret, U. Ebels, K. Ollefs, F. Wilhelm, A. Rogalev, and W. E. Bailey, *Phys. Rev. B* **94**, 014414 (2016).